Shape optimization of a long tapered R134a ejector mixing chamber

José Sierra-Pallares[a,b,*], Javier García del Valle[c], Jorge Muñoz Paniagua[d], Javier García[d], César Méndez Bueno[a], Francisco Castro[a,b]

[a]*Departamento de Ingeniería Energética y Fluidomecánica, Escuela de Ingenierías Industriales. Universidad de Valladolid - Paseo del Cauce 59, 47011 Valladolid, Spain*
[b]*Instituto de Tecnologías Avanzadas de la Producción. Universidad de Valladolid - Paseo del Cauce 59, 47011 Valladolid, Spain*
[c]*Facultad de Ingeniería Civil y Mecánica. Campus Huachi. Universidad Técnica de Ambato. Av. Los Chasquis y Río Payamino 180206 Ambato, Ecuador*
[d]*Departamento de Ingeniería Energética, Escuela Técnica Superior de Ingenieros Industriales. Universidad Politécnica de Madrid - C/ José Gutiérrez Abascal 2, 28006 Madrid, Spain*

Abstract

The purpose of this investigation is to develop a computational methodology for the shape optimization of long-tapered mixing chambers of refrigerant ejectors based on the internal entropy generation. The workflow of the aforementioned methodology includes a one dimensional model to generate a baseline geometry. Then a design of experiments is performed around a parametrization of the baseline geometry and the resulting combinations are introduced in the CFD model. Based on the CFD entropy generation results, a surrogate model is trained and further used to determine the optimum geometry for the mixing chamber. The application of the surrogate model is not straightforward, but rather a loop style routine has been programmed in order to assure a global minimum rather than a local one. The proposed methodology has been applied to a R134a ejector geometry previously studied by the authors both experimentally and numerically. It has been found that given a design critical point, the entrainment ratio may be increased up to a value of 16discharge pressure remains constant.

Keywords: CFD, ejector, mixing chamber, refrigeration, shape optimization

1. Introduction

An ejector is a simple device in which a high pressure stream (primary fluid) is used to compress a low pressure stream (secondary fluid) to a higher pressure (discharge pressure). A number of ejector systems have been developed for its use in refrigeration applications [1], where at least eight different cycles are identified. In this investigation, a single ejector refrigeration system is considered. In this configuration, a refrigerant stream of low velocity and lowpressureis evaporatedtogenerateacoolingcapacity, and compressed to an adequate condensation pressure level by the interaction with a high velocity stream generated byheat input and adiabatic near-reversible expansion [2]. Its low coefficient of performance (COP) has led the current trends in supersonic ejector research towards minimizing the ejector internal irreversibility [3].

*Corresponding author
Email address: jsierra@eii.uva.es (José Sierra-Pallares)

However, a shift towards the use of ejectors as expansion valves in transcritical CO2 cycles has renewed the investigation in ejector technology, mainly for two reasons. The first one is related to the energy recovery potential from throttling losses in the aforementioned cycles. The second one is related to the wide scale reintroduction of CO2 enforced by the phase out of HFC refrigerants, in Europe by the MAC directive and the F-Gas regulation [4] and internationally by the Kigali amendment of the Montreal protocol [5]. The results of the former normative have been uneven across different geographic areas. For commercial refrigeration, whereas northern countries have seen a massive coming back of CO2, southern countries are and will be struggling by either cascading CO2 with other refrigerant in the high temperature side or using indirect loop ammonia systems. For industrial refrigeration, ammonia is the ultimate winner. In between, HFO based refrigerants will be introduced in a number of applications, from automotive air conditioning to commercial applications in competition with the CO2. Its market penetration will ultimately depend on its price, being currently dictated by a monopolistic criteria. In this scenario HFO-1234yf is proposed as a substitute of HFC-R134a, used in this investigation. Three reasons motivate the election of HFC-R134a, (1) experimental data for supersonic ejectors against which validate the CFD model is currently unavailable for HFO-1234yf, (2) the optimization routine presented is independent of the refrigerant used and (3) is theorized that a limited entrainment ratio enhancement, as concluded in this investigation, is extensible to other refrigerants, based on the results obtained by Ref. [6], where a comparative of the ejector entrainment ratio for different operating conditions of up to nine refrigerants is presented which resulted in similar patterns regardless of the refrigerant.

In order to design and develop a high performance ejector, a clear understanding of the entropy generation sources inside the ejector is needed. To this end, several studies have addressed the modelling and simulation of ejectors using different approaches. One dimensional models provide fast computation of global statespace variables based on simplifying hypotheses about the flow behaviour. However, it is commonly accepted that these models are not sufficient to understand the physics of a supersonic ejector. Some authors claim that these models only can be used when the ejector is operated at its critical conditions [7], and they do not provide detailed spatial information about the location of irreversibilities. On the other hand, Computational Fluid Dynamics (CFD) models are able to provide a detailed description of the flow physics inside the ejector. Generally speaking, CFD models are accurate enough for providing the essential information for engineering purposes [2,8] with a reasonable computational cost.

In the last years, a number of studies have been conducted towards the exploration of the irreversibility sources inside the ejector to look for possible design improvements. Croquer et al. [9] perform a CFD computation of an ejector previously studied experimentally by Garcia del Valle et al. [3], and perform an exergetic study using the indirect method [10]. Their analysis of the exergy looses shows that the main locations of entropy generation are downwards the nozzle exit, thus located in the mixing chamber and the diffuser. Similar results are reported by Banasiak et al. [11], also using the indirect method. Lamberts et al. [12] perform an irreversibility analysis of ejectors using energy and exergy tubes, connecting the sources of irreversibility to the entrainment

and therefore the boundaries of the computational domain. A breakthrough for the analysis of entropy generation inside ejectors was performed by Sierra-Pallares et al. [13], who employed the direct method -the entropy transport equation in differential form-to determine a very detailed map of entropy generation inside the ejector. That approach also allows to distinguish the sources of irreversibility, and the mechanisms underlying the entropy generation in each case. Their results show that, for different mixing chambers, the fluctuating viscous dissipation accounts for more than 75shear layer after the nozzle exit and the shock wave train, independently of its position.

These previous studies open the door for the design of ejector geometries with minimum entropy production. However, relatively little research has been reported in the open literature concerning shape optimization of ejectors. To our knowledge, only three papers are available, all of them concerning to multiphase ejectors. Concretely, the works of Palacz et al. [14,15] refer to the shape optimization of a CO2 ejector used in supermarket refrigeration systems. Two optimization algorithms, a genetic algorithm (GA) and an evolutionary algorithm (EA), were used with a validated CFD model based on the homogeneous equilibrium model (HEM). The optimization results showed that the ejector efficiency may be improved by 6of the considered ejectors, and resulted in a smoother expansion inside the motive nozzle, less intense turbulence and a more uniform velocity field inside the mixing chamber. Lee et al. [16] tackle the shape optimization of a two phase R600 ejector using a homogeneous, non-equilibrium, two-phase flow computational fluid dynamics (CFD) model. The model is first validated with experimental data and, after that, the design parameters of the ejector are optimized using a multi-objective genetic algorithm (MOGA) with an on-line approximation-assisted optimization (OAAO) approach to find the geometry with the best performance.

Previous published studies are limited to ejectors working with two phase flow, and although its methodologies can be adapted, current literature lacks the use of surrogate models, or objective functions able to work with the entropy generation rate inside the ejector. While some research has been carried out on shape optimization of ejectors, there is still very little scientific understanding of the problem. The purpose of this investigation is, given a set of boundary conditions for the ejector, to present a complete methodology in order to obtain the geometry that generates the lowest entropy, thus maximizes the mass entrainment ratio. The aforementioned procedure has been applied to the R134a ejector chamber previously studied both experimentally [3] and numerically [2,13], which is originally designed to favour recompression and mixing.

Given a target operational point, the optimization procedure is initialized with a baseline geometry generated using a one dimensional model. An entropy minimization routine which couples a design of experiments stage, advanced surrogate modelling and CFD simulations has been implemented in order to obtain the optimized geometry. A commercial CFD and optimization suite (ANSYS Workbench) has been used in this investigation.

2. Methodology

In this section, the complete methodology for the optimization of the mixing chamber of a HFC-R134a ejector is presented. Before going into a detailed introduction of the optimization method, the starting point of the description of our methodology is the definition of the optimization problem, i:e: specification of the boundary conditions in terms of pressure and temperature for the primary and secondary streams of the ejector and the generation of the baseline geometry. For the former, we have chosen similar conditions to those depicted in our previous studies [3,13]. These values are shown in Table 1.

The outlet pressure is fixed to 8.15 bar, being this value the critical pressure for the baseline ejector geometry. This is further discussed in Section 3. It is worth to note here that these conditions remain constant for the whole set of calculations performed in this work.

[Table 1 about here.]

The discharge pressure value chosen for the optimization will be discussed later. Once this step is achieved, a one dimensional model [13] is used to generate the baseline geometry that will be optimized.

2.1. Baseline geometry generation

[Figure 1 about here.]

In this section, guidelines to develop a baseline geometry from a prescribed boundary conditions are proposed. Some comments are necessary in order to understand some criteria in which the baseline geometry is based upon:

1. Commonly, one-dimensional models have been used for the purpose of predicting the ejector entrainment ratio. However, it will be shown that with little modification such models may be adapted to obtain a baseline geometry given the boundary conditions.
2. As discussed on previous investigations [3], a possible way of ejector performance enhancement may be obtained by means of a tapered mixing chamber which promotes supersonic compression. As is the case for the secondary throat in supersonic wind tunnel design, the constant area section is partially substituted by a variable area region. The role of this region is to decelerate the flow to the sound speed at the Mach 1 section. A cone shape supersonic converging diffuser is considered for this purpose. Two reasons suggest the use of a simple geometry. In the first place, if the device were to be machined, curved shapes in a small inner diameter may be impractical. In the second place, much work was done in supersonic air ejectors in the post-war era. In a paper by Ginoux [17] the effect of the inlet geometry for an air ejector is conducted. It is concluded that in the absence of secondary flow, pressure recovery for a tapered inlet is higher than for a constant area ejector. Furthermore the effect of the conical angle is studied for a number of nozzles, concluding that the optimal angle is a function of the Mach number. Thus, the inlet geometry chosen for the present investigation is based upon these assumptions.

3. Regarding the nozzle design for ejector applications, cone shaped types are commonly used and little effort has been paid to the design of shock free supersonic nozzle, partly because it is not easy to manufacture small inner geometries. However, for aeronautical purposes, well designed nozzles are in used, being the work of [18] the only reference found in which an innovative manufacturing process for small nozzles is described and experimentally tested. The difficulties found in obtaining an ideally-expanded nozzle are explicitly cited in his investigation. In fact, to the best of the authors knowledge, there is not in the literature any reference in which a systematic approach of the influence of the nozzle design into the inner entropy generation and thickness of the shear layer in the entrained region are provided.

Based on the previous comments, two things are needed (1) a parametrized schema of the baseline geometry which takes into account the aforementioned criteria, Fig. 1, and (2) and a onedimensional model adapted for that particular schema. In this case the model developed by Garcia del Valle et al. [19] will be used. This model computes the evolution of a supersonic stream issuing from a nozzle in a variable pressure atmosphere. A model adaptation is needed in order to account for the long tapered region, thus Fig. 2 has been included. It is important to note here that the model is adapted to design an ejector operating in the critical point.

For the model adaptation, the starting point is a constant area section (upper half of the figure), where a normal shock occurs at the end of the constant area section. This constant area section is partially substituted by a variable area region (Region IV in the picture). This region role is to decelerate the flow to the sound speed at the Mach 1 section (section ss). Provided the one dimensional model computes the primary and secondary mass flow as well as the flow thermodynamic properties at the critical section, an extension is needed to represent Region IV behaviour. As an approximation, instant mixing is proposed, leading to uniform properties immediately downstream the critical section (velocity v_{mix}, enthalpy h_{mix} and density ρ_{mix} according to Eqs. (1)-(4)) followed by an isentropic compression in order to compute the properties at the Mach 1 section, Eqs. (5) and (6), in which the secondary throat area (A_{ss}) and the density at the sound speed rss are solved for. Immediately upstream the instant mixing the properties are denoted as m, mix and e, mix for the primary and secondary stream respectively. Furthermore, it is important to note the summation in Eqs. (1) and (2), since the model discretize the primary fluid in the radial direction.

[Figure 2 about here.]

$$\dot{m}_1 \cdot v_1 + \dot{m}_2 \cdot v_2 = (\dot{m}_1 + \dot{m}_2) \cdot v_{mix} \tag{1}$$

$$\dot{m}_1 \cdot \left(h_1 + \frac{v_1^2}{2} \right) + \dot{m}_2 \cdot \left(h_2 + \frac{v_2^2}{2} \right) = (\dot{m}_1 + \dot{m}_2) \cdot \left(h_{mix} + \frac{v_{mix}^2}{2} \right) \tag{2}$$

$$(\dot{m}_1 + \dot{m}_2) = \rho_{mix} \cdot A_{crit.section} \cdot v_{mix} \tag{3}$$

$$s_{mix} = f(\rho_{mix}, h_{mix}) \tag{4}$$

$$h_{mix} + \frac{v_{mix}^2}{2} = h_{ss}(s_{mix}, \rho_{ss}) + \frac{ss(s_{mix}, \rho_{ss})^2}{2} \tag{5}$$

$$(\dot{m}_1 + \dot{m}_2) = \rho_{ss} \cdot A_{secondary\ throat} \cdot ss \tag{6}$$

The sound speed and the enthalpy at the sound speed are computed implicitly from the entropy and ρ_{ss}. Furthermore, the critical back pressure may be computed if the isentropic stagnation pressure of mixed flow is computed.

In order to have an explicit solution, some model parameters have to be set according the following rules:

1. Angles α_1 and α_3 and length L_2 are not model parameters. They are set according the values shown in Fig. 1.
2. Angle α_2 and length L_1 are model parameters. But their influence is negligible due to the isentropic evolution of the flow. They are also set. The CFD based optimization presented in the present investigation is a step towards quantifying the contribution of this parameters.
3. Regarding the nozzle exit position, the application of one dimensional model results into higher entrainment ratios and lower discharge pressures for the critical point when the nozzle is retracted. Since the evolution of the flow in the mixing chamber is supposed isentropic, there is no trade off regarding NXP position and the entropy generation regarding the one dimensional model. However, high values of the NXP parameter in Fig. 1 would probably yield not accurate one dimensional models results, since viscous effects not considered by the model are not negligible. Thus, an NXP value of 1mm based on the experimental results found in Ref. [3] was chosen for the baseline geometry.

[Table 2 about here.]

With this modifications, geometrical parameters $H1$, $H2$, $H3$ and $H4$ may be derived from the model if:

1. The application motive power is known. This data is used to compute $H3$.
2. The motive nozzle is supposed to be adapted. The model can compute the pressure of the secondary fluid and the outer cell of the primary fluid at the nozzle exit. Those values have to be equal.
3. The model can compute the area of the secondary throat (*ss* section) which will yield $H2$.
4. The critical pressure is known since the boundary conditions are set. Parameters $H1$ and $H2$ will be mainly dependent on the critical pressure.

The result is a 4×4 nonlinear system which can be solved for. This system is shown implicitly in Eqs. (7)-(10). This procedurewas previously applied to the design of one of the geometries shown in Garcia del Valle et al. [3], that will be used as baseline geometry here. The baseline values for the parameters considered for the optimization algorithm are included in the legend of Fig. 1.

A view of the complete computational domain considered for the baseline geometry is shown in Fig. 3.

2.2. Shape optimization method

After having introduced the baseline geometry generation, here we describe the methodology used for solving the optimization problem itself. The optimization method selected to solve this problem is the genetic algorithm (GA). GAs, introduced by Ref. [20] and developed by Ref. [21], are a technique that mimics the mechanism of the natural evolution. Once a population of potential solutions is defined, three operators (selection of the fittest, reproduction or crossover and mutation) are applied. Iteratively, a new population is generated and better results are obtained until a solution closer to globally optimal solution is reached. The combination of survival-of-the-fittest concept to eliminate unfit characteristics with a random information exchange and the exploitation of the knowledge contained in old solutions permit GA to effect a search mechanism with efficiency and speed. GAs are englobed in zero-order methods, based on direct evaluations of the objective function (the concept of objective function, and its particular definition for this problem, is addressed in section 2.2.4). This is an advantage compared to first-order methods that need the calculation of the first derivative of the objective function. However, the large number of evaluations required when using GA is a disadvantage that minimizes its power. Furthermore, this behaviour is emphasized in this case, where a turbulent, unsteady, compressible flow imply an additional computational cost.

The problem of the large number of evaluations required by the GA directly depends on the dimensionality of the design space. So, the number of design variables introduced in Fig. 1 helps minimizing such drawback. Nevertheless, a further reduction in the computational cost of GA is achieved by using a surrogate model. Typically, each evaluation of the objective function within the GA refers to a CFD simulation, but even the present increase of the computational power is not sufficient to conceive a thorough search of the design space using only accurate simulations. This situation leads to the introduction of an approximate model whose computational cost is much lower than the CFD simulation. In Fig. 4, a conventional optimization work-flow is represented. This scheme refers to an on-line optimization where, after the end of the GA optimization process, the best solution found by the surrogatebased optimizer (candidate point) is evaluated and verified, and this new simulation is added to the initial database thatwas used to train or fit the coefficients of the surrogate model. A similar workflow to that showed in Fig. 4 is implemented in ANSYS DesignXplorer, where we use the Multi-Objective Genetic Algorithm (MOGA) for the optimization.

[Figure 3 about here.]

2.2.1. Surrogate model

A very large variety of surrogate models are available, and more sophisticated and computational expensive surrogate models have become popular. In most cases, it is the experience what drives the choice of a particular surrogate model, like in Viana et al. [22]. Indeed, there is not any surrogate model that works better than others in general but depending on the application, as the parametric study presented by Jin [23] concludes. To deal

with the choice of a specific metamodel technique, in this work we consider the Genetic Aggregation response surface model as the surrogate model, which is implemented in ANSYS DesignXplorer. It involves a combination of several metamodels, namely a second-order polynomial, a non-parametric regression model, a kriging model and moving least squares method, weighted by a corresponding parameter, so that:

$$\hat{y}_{ens}(x) = \sum_{i=1}^{N} w_i \hat{y}_i(x), \tag{7}$$

where $\hat{y}_{ens}$ is the prediction of the ensemble; $\hat{y}_i$ is the prediction of the i-th metamodel; N is the number of metamodels used and w_i is the weight factor of the i-th metamodel. To select the best combination of metamodels, the Genetic Aggregation uses a genetic algorithm that generates successive populations of potential optimal response surfaces. The fitness function to determine the best one (*i.e.*, to estimate the best weight factor values) takes into account both accuracy in the approximation of the training points and generalization of the prediction ability. For this, ANSYS DesignXplorer minimizes the Root Mean Square Error (RMSE) of the Design of Experiments [22,24].

2.2.2. Design of Experiments

The surrogate model is constructed with a sampling plan of the design space. This sampling plan is called Design of Experiments (DoE), and will be used to fit the parameters and weights of the surrogate model. The technique chosen to generate the DoE is the Latin Hypercube Sampling (LHS) [20]. In this step, the feasible regions for each design variable ($\mathcal{L}_i$) should be specified. The criterion we have adopted consist of perturbing each geometric value a 20% for its baseline value $\bar{L}_i$,

$$\mathcal{L}_i = \left[\bar{L}_i - 20\%,\ \bar{L}_i + 20\%\right]. \tag{8}$$

This criterion is based in the results reported by Palacz et al. [10], where the optimum geometry parameters differed by around 30 - 40% from its baseline values. We have chosen a more conservative ±20% threshold to avoid convergence problems during the CFD calculation, but if the optimal solution saturates the design space, a further augmentation of the design space is feasible.

The number of samples should be large enough for the algorithm to be able to produce a reliable surrogate model training. Here, the initial DoE size is set to 50, following the criterion of Loeppky et al. [21] of $S = 10n$, where n is the dimensionality of the design space.

For each experiment generated by the DoE, the ANSYS Design- Modeler tool is called. Using the geometric data provided for each design point, a complete axisymmetric model of the ejector is developed similar to those used before by our group [2,13]. Once the geometry is generated, it is fed to the ANSYS Meshing tool. In this step, a non structured mesh is generated automatically.

2.2.3. CFD model

The CFD model employed in this work has been previously described and validated by the authors thoroughly [2], and it will be commented briefly here: that model consisted of the Standard k - ? model of turbulence along

with the REFPROP library to compute thermodynamic and transport properties [27]. The validation of the model was carried out by comparison to local pressure measurements along the wall of the ejector besides of the classical validation using the mass entrainment ratio. This was done to ensure the flow field was correctly predicted. The mean average deviation found between the model and the experimental mass entrainment ratio was around 16%.

In this work, however, an alternative set of models to REFPROP have been used to increase the robustness and reduce the computational cost of the CFD computation without compromising its accuracy. Namely, thermodynamic modelling has been substituted by the Peng-Robinson equation of state (PREOS) to compute thermodynamic variables [28] and the Chung method [29] for computing transport properties. The former gives the computation of enthalpy, heat capacity, density and other thermodynamic properties, and the latter gives thermal conductivity and viscosity. The comparison between the REFPROP library and PREOS has been tackled in the past by other authors [8,30] and insignificant differences were found. Regarding transport properties, the Chung method is proven to be accurate enough for dense gases [31], and their influence on the final flow field is small due to the effect of turbulent viscosity as shown by Croquer et al. [8]. This modification allows to reduce the computational cost because of the relative simplicity of the PREOS versus the REFPROP library and the possibility of use a higher Courant numbers without stability problems. A density-based solver and an implicit formulation is used, along with a second order discretization. In the density-based approach, the continuity equation is used to obtain the density field while the pressure field is determined from the equation of state. A variable Courant number (Co) strategy is employed, being Co ≈ 1 at the beginning of the computation and increasing its value until Co $= 30$ at 30000 iterations. This scheme has proved to be satisfactory for all of the cases under study in this work, being the typical run time about 1900 s on an Intel i7 12-core machine with 64 GB of RAM.

A non-structured axisymmetric mesh composed by quadrilaterals cells has been used. Near wall region is refined in order to obtain an average $y^+ \approx 125$, since the wall boundary condition used is the standard wall function. Furthermore, the nozzle throat as well as the start of the diffuser have been refined in a dynamic way to ensure mesh independent results. Several dynamic mesh refinements are tackled, each one every 6000 iterations, based on a Mach number gradient criterion. Although some of them are not necessary, this guarantees mesh independent results. This is clearly seen in Fig. 5a where the entropy generation rate Vs. the iteration number for a typical run for the baseline is shown. Additionally, Fig. 5b shows the evolution of the mass flow rate through the secondary stream inlet Vs. iterations numbers, indicating the mass balance is fulfilled shortly after the second refinement. A very good convergence is found with less than 30000 iterations. The mesh employed for running this benchmark is shown in Fig. 6. The mesh is very refined close to the walls and shock waves. The typical case contains about 50000 cells.

The post - processing step is performed by computing the entropy generation inside the computational domain. The entropy in a flow field is a state variable that in its specific form has a balance equation that, for a single phase, non-reacting and single component flow reads [27]:

$$\rho \frac{Ds}{Dt} = -\nabla \cdot \left(\frac{\mathbf{q}}{T}\right) - \frac{1}{T^2}\mathbf{q} \cdot \nabla T - \frac{1}{T}\boldsymbol{\tau} : \nabla \mathbf{v} \tag{9}$$

which can recast into

$$\rho \frac{Ds}{Dt} = -\nabla \cdot \boldsymbol{\sigma} + s_g \tag{10}$$

Where $\boldsymbol{\sigma}$ is the entropy flux vector and s_g is the entropy generation rate per unit volume. A comparison between (9) and (10) leads to

$$\boldsymbol{\sigma} = \frac{\mathbf{q}}{T} \tag{11}$$

$$s_g = \frac{1}{T^2}\mathbf{q} \cdot \nabla T - \frac{1}{T}\boldsymbol{\tau} : \nabla \mathbf{v} \tag{12}$$

It can be observed that the total entropy generation rate can be splitted in two contributions, each one strictly related to a specific transport phenomenon: a contribution due to heat transfer (14) and a viscous dissipation term (15):

$$s_g = s_g\big|_h + s_g\big|_\mu \tag{13}$$

where

$$s_g\big|_h = \frac{1}{T^2}\mathbf{q} \cdot \nabla T \tag{14}$$

$$s_g\big|_\mu = -\frac{1}{T}\boldsymbol{\tau} : \nabla \mathbf{v} \tag{15}$$

In a turbulent flow, Equation (9) has to be time averaged in order to find an equation for the mean entropy. For a compressible flow, Favre averaged is employed to obtain

$$\bar{\rho} \frac{D\tilde{s}}{Dt} = -\nabla \cdot \widetilde{\boldsymbol{\sigma}} - \bar{\rho}\left(\frac{\partial \widetilde{u''s''}}{\partial x} + \frac{\partial \widetilde{v''s''}}{\partial y} + \frac{\partial \widetilde{w''s''}}{\partial z}\right) + \widetilde{s_g\big|_h} + \widetilde{s_g\big|_\mu} \tag{16}$$

Unclosed terms are modelled using the method proposed by Herwig and Kock [6]. The entropy generation rate is divided between the contribution of the mean gradients and the contribution of the fluctuating components:

$$\widetilde{s_g\big|_h} = \left\langle s_g\big|_h \right\rangle_{mean} + \left\langle s_g\big|_h \right\rangle_{fluc} \tag{17}$$

$$\widetilde{s_g\big|_\mu} = \left\langle s_g\big|_\mu \right\rangle_{mean} + \left\langle s_g\big|_\mu \right\rangle_{fluc} \tag{18}$$

where the contibutions to the entropy generation rate due to mean gradients are:

$$\left\langle s_g\big|_h \right\rangle_{mean} = \frac{\kappa}{T^2}\left[\left(\frac{\partial \tilde{T}}{\partial x}\right)^2 + \left(\frac{\partial \tilde{T}}{\partial y}\right)^2 + \left(\frac{\partial \tilde{T}}{\partial z}\right)^2\right] \tag{19}$$

$$\left\langle s_g\big|_\mu \right\rangle_{mean} = \frac{\mu}{T}\left[2\left\{\left(\frac{\partial \tilde{u}}{\partial x}\right)^2 + \left(\frac{\partial \tilde{v}}{\partial y}\right)^2 + \left(\frac{\partial \tilde{w}}{\partial z}\right)^2\right\} + \left(\frac{\partial \tilde{u}}{\partial y} + \frac{\partial \tilde{v}}{\partial x}\right)^2 + \left(\frac{\partial \tilde{u}}{\partial z} + \frac{\partial \tilde{w}}{\partial x}\right)^2 + \left(\frac{\partial \tilde{v}}{\partial z} + \frac{\partial \tilde{w}}{\partial y}\right)^2\right] \tag{20}$$

and the fluctuating ones are:

$$\left\langle s_g\big|_h \right\rangle_{fluc} = \frac{\alpha^T}{\alpha} \left\langle s_g\big|_h \right\rangle_{mean} \tag{21}$$

$$\left\langle s_g\big|_\mu \right\rangle_{fluc} = \frac{\bar{\rho}\varepsilon}{\tilde{T}} \tag{22}$$

Although equations (19) - (22) can be used in every point of the computational domain, special care is needed when using wall functions in the computation of the turbulent flow. In this work, standard wall functions are used and in order to obtain the correct estimation of entropy generation in the cells adjacent to the walls using the method proposed by Walsh and McEligot [28].

In a standard computation, the continuity, momentum and energy equations are first solved. Then, in a postprocessing step, the entropy generation is computed at cell centers except in the first row of cells adjacent to the wall, where the contribution due to the standard wall function is applied. Upon that, in every cell of the computational domain, a value for $\widetilde{s_g\big|_h}$ and $\widetilde{s_g\big|_\mu}$ is found. The complete entropy generation for the whole geometry, $\mathcal{S}_{gen}$ is thus obtained doing the summation of the volumetric entropy generation for all the control volumes, and the total entropy generated for every design point is evaluated as:

$$\mathcal{S}_{gen} = \sum_i^N \left(\widetilde{s_g\big|_h} + \widetilde{s_g\big|_\mu} \right)\Big|_i V_i \tag{23}$$

where V_i is the volume of each computational cell and N the number of cells. A complete description of the application of the above equations to a CFD model of an ejector is found in a previous work by the authors [9].

Although the above computation may appear cumbersome, the current implementation is efficient and the entropy generation map is computed after the last iteration of the CFD computation with negligible computational effort.

2.2.4. Objective function

The entropy generation inside the computational domain, Eq. (23) is chosen as objective function for the online optimization,

$$\min_{L_i} \left(\mathcal{S}_{gen} \right) \qquad \text{s.t.} \qquad L_i \in \mathcal{L}_i \tag{24}$$

where $\mathcal{L}_i$ are the respective feasible regions of the decision or design variables.

It is worth here to comment that mass entrainment maximization and entropy generation minimization are equivalent as objective functions. Nevertheless, there is a subtle different between them. Whereas the mass entrainment ratio is a macroscopic parameter, the entropy generation is a local one, allowing for the shape optimization of just a part of the ejector rather than the whole geometry. Therefore, the algorithm will look for a geometry that minimizes Eq. (28) taking fixed boundary conditions, which are those specified in Table 1 and a discharge pressure of 8.15 bar. To verify if the generated geometry from the algorithm is optimal, the total entropy generation for each design point between consecutive iterations is chosen as stop criterion:

$$\left| \dot{S}_{gen}^{k} - \dot{S}_{gen}^{k-1} \right| < \varepsilon \tag{25}$$

where $\varepsilon = 0.005\ \mathrm{W\,K^{-1}}$.

The computational tool described in this section is called UVaEjector [34], and it is openly available under a CC-BY-4.0 license.

[Figure 4 about here.]

3. Analysis of the baseline geometry

[Figure 5 about here.]

In this section we analyse the baseline geometry in detail. Since the aim of this work is to produce an optimal shape for the mixing chamber of a R134a ejector, we need to specify a discharge pressure to carry out the CFD computations and the shape optimization. In Section 2.1 we have chosen a value of 8.15 bar for the discharge pressure. This choice is based on the entrainment ratio - discharge pressure diagramfor the baseline geometry obtained using the CFD model (Fig. 7). The data is obtained by fixing the boundary conditions at both inlets (see Table 1) of the ejector and varying the discharge pressure. Fig. 7a depicts the critical point at a discharge pressure of 8.15 bar. Fig. 7b shows the total entropy generated for each value of the discharge pressure. As discussed in our previous publication [13], the critical point is also a minimum entropy generation point. It is worth noting how is the distribution of entropy generation along the ejector for discharge pressures (p_D) above (off-design, $p_D = 8.30$ bar) and below (on-design, $p_D = 8.00$ bar) the critical point. Fig. 8 shows the entropy generation maps for on-design conditions, critical conditions and off-design conditions respectively. As it can be seen, when working at on-design conditions (Fig. 8a) the principal entropy generation sources are the mixing between primary and secondary fluid streams and a normal shock wave obtained at the section change between the constant area chamber and the diffuser, slightly downwards the constant area section. This study reveals that when the critical pressure is reached (Fig. 8b) the latter contribution to entropy generation is eliminated and the normal shock is very weak. If the discharge pressure is increased further, the irreversibilities grow in the mixing area because of the difference in momentum between both streams increases and the higher the velocity gradient between the primary and secondary fluid, the higher would be the viscous forces, thus the entropy generated. The dominating mechanism leading to entropy production in all cases is the fluctuating viscous dissipation [13]. These aspects are better visualized using a one - dimensional plot such that of Fig. 9. It depicts the entropy production per unit length. This figure is produced integrating the entropy generation map at constant axial coordinate surfaces along the computational domain. The figure reveals that, for the nozzle region, entropy generated is very similar in spite of the discharge pressure. This is due to the fact that entropy production is located in the boundary layer of the nozzle, where a sharp gradient exists.

[Figure 6 about here.]

[Figure 7 about here.]

Since the flow is completely choked in the nozzle and the boundary conditions for the primary inlet are equal in all the simulations analysed here, entropy generation is the same. However, at on-design conditions, the sharp peak depicted in the figure shows how the irreversibility is concentrated in the shock train region and the normal shock wave. For the critical condition and off - design condition, the main irreversibility source is the shock train region. From the results above, it can be inferred that entropy generation maps using the long-tapered mixing chamber proposed in this work are characterized by a heavy entropy generation rate in the mixing region but relatively weak or non-existing entropy generation in a normal shockwave downwards the mixing area when the discharge pressure is the critical pressure. In order to minimize the entropy generation, aside from the inlet conditions (pressure and temperature) the discharge pressure must also be fixed to the problem to be fully defined. The above results suggest that the optimization algorithm will yield a geometry that operates very close to the critical point, since it is the point where entropy generation is minimum for a given geometry. Thus, in order to compare with the baseline geometry it is advisable to choose the discharge pressure corresponding to the baseline critical point. In this way, any increase in entrainment ratio will be easily identified. Therefore, a value of 8.15 bar is fixed as discharge pressure from this point onwards. For this particular case, Fig. 9, the entropy generation in the motive fluid supersonic core is negligible, being the bulk of the entropy generation located in the mixing layer between the primary and secondary fluid, mainly due to fluctuating viscous dissipation. Either a slight overexpanded or underexpanded nozzle would contribute little to the entropy generation mechanism depicted above provided that strong shock are not formed in the motive fluid core. For this reason, nozzle optimization has not been included in the present model. In this regard, geometry parameters used in the one dimensional model introduced in section 2.1. were chosen in order to obtain an adapted nozzle. This approach is successful, as minimal entropy generation is found in the supersonic core region downstream the nozzle in Fig. 8.

4. Shape optimization

In this section we show how the on-line optimization process is made. Following the flow chart depicted in Figure 3, a design of experiments (DoE) is carried out around the baseline geometry. As commented before, we choose to add a perturbation of ±20% to each geometrical parameter defining the mixing chamber to fix the upper and lower limits of the design space. The results are found in Table 3.

[Table 3 about here.]

Once the design space is bounded, the LHS is used to generate the set of 50 experiments that fill the design space. When the experiments are available, ANSYS Workbench automatically builds up the corresponding geometry and mesh, and run the case using the methodology described in Section 2.3. When each run is finished,

the entropy generation and the secondary mass flow rate are available for each experiment. Table 4 shows these results.

[Table 4 about here.]

Those experiments with negative secondary mass flow rate are not appropriate for the training of the surrogate model and are eliminated from the design space to ensure the surrogate model is only fed with physically meaningful solutions. Although the entropy generation analysis shows these cases are possible (entropy generation is positive in all of them), the boundary condition fixed at the secondary mass flow rate inlet is not adequate to deal with negative values of the mass flow. Thus, these results are not fully reliable from a physical point of view.

The surrogate model is now trained with the reliable CFD results and the optimization algorithm is run. The optimization algorithm gives a candidate point with minimum entropy generation according to the surrogate model. To ensure this optimum is a global one and not a local one, it is added to the design space as a new experiment. Then the process is repeated: the new experiment is run with the CFD model and its output used to train further the surrogate model providing a new candidate point with the optimization algorithm. This process is repeated until there is a small difference in entropy generation between two consecutive candidate points ($\epsilon = 0.005$ W K^{-1}). This on-line optimization is described in Table 5. The table shows how in just 6 iterations the method show convergence.

[Table 5 about here.]

As a result, a global optimum in relation to the design space limits, E56, is reached. Then, the methodology needs 56 evaluations of the CFD model, which roughly corresponds to $\approx$ 30 CPU hours of computation in an Intel i7 machine working with 12 cores. Table 5 also show a range of geometries where the entropy generation rate is close to the optimum. Experiments E53 to E56 show a very similar entropy generation rate and therefore a high entrainment ratio.

The accuracy of the surrogate model is quantified using the goodness of fit. Figure 8 shows the entropy generation rate computed with the CFD model along with that computed using the surrogate model. A R-squared value of 0.993 is found, guaranteeing the quality of the emulation within the limits of the design space.

[Figure 8 about here.]

5. Discussion

5.1. Differences between baseline and optimized geometries

In the next paragraphs, we proceed to describe the main differences found between the optimized and baseline geometries. Figure 9 over-impose both geometries in the same picture to show the main differences. Table 6 shows the value of each dimension along with the secondary mass flow rate and the entropy generation rate.

[Table 6 about here.]

[Figure 9 about here.]

It is shown that the optimized geometry is not very different from the baseline one, being the bigger differences the values of L1, L2 and H1, which are significantly lower. However, this result confirms the one dimensional model presented is able to produce a design close enough to the optimum one using much lower computational requirements. This result suggests the hypothesis the one dimensional model are based on are essentially correct. However, it is worth noting the influence of the constant area region is not negligible, and this geometrical dimension cannot be specified by the one dimensional model. If we focus on the increase in secondary flow rate, it is around 16%, thus entrainment ratio and COP of the refrigeration system is increased in the same amount.

It is worth here to explain that these results should be understood in terms of trends. The CFD model itself is validated with an absolute average deviation of 16% Vs. experimental entrainment ratio found [2]. An increase in 16% in entrainment ratio while conserving the critical pressure means that the optimized geometry should have an experimental entrainment ratio significantly superior the baseline.

Figure 10 shows the entrainment ratio Vs. discharge pressure for both the baseline and the optimized geometries. The critical pressure is approximately similar for both sets of data, although the optimized one is shown to be slightly higher (8.15 and 8.18 bar respectively), indicating the optimized geometry is slightly sub-optimal. Nevertheless, this result is in complete accordance with our previous analysis: the baseline discharge pressure will become the critical point pressure in the optimized geometry.

[Figure 10 about here.]

Regarding the axial entropy generation rate, Figure 11 depicts the comparison between the optimized and the baseline geometry. Since the flow in the nozzle is completely parabolic, the entropy generation rate is equal in both geometries inside it. It is worth pointing here that most of the entropy generation is produced after the nozzle exit, being its effect on the overall entropy production very small. From the nozzle exit onwards, the main differences arise in the distribution of the entropy generation. The baseline geometry shows an individual peak corresponding to the mixing zone between the primary an secondary flows. The optimized one shows a double peak, indicating the entropy generation is not only located in the convergent part of the mixing zone, but also in the constant area part and the diffuser.

[Figure 11 about here.]

This result is much better visualized with the contour maps of entropy generation and pressure distribution. Fig. 14a shows the entropy generation map for the baseline and the optimized geometries. The plot is depicted in a way the baseline geometry is located in the lower side of the figure and the optimized one in the upper side, for a better comparison between them. The bulk of the entropy generation is located in the shear layer between the primary and secondary fluid, however, in the optimized geometry irreversibilities are reduced in this area. If the absolute pressure distribution is considered, Fig. 14b, two features are worth to be discussed. First, the optimized geometry produces an oblique shock at the start of the diffuser, however the resulting increment in the rate of entropy generation is offset by the reduction accomplish in the shear layer region. This phenomena is visible in Fig. 13, related to the local maxima at a coordinate of 0.05 m. This result suggests that the optimized geometry found here is slightly sub-optimal. The second one is related to the flow downstream the nozzle, a topic already mentioned in the description of the baseline geometry. As shown in the pressure distribution, the nozzle is slightly underexpanded, producing a train of oblique shocks, yet their contribution to the entropy generation is minimal. In order to better understand the inner core behaviour, the axial distribution of pressure along the centerline has been included, Fig. 14. Both geometries share a similar pattern. It is important to note that the pressure tends to increase in the convergent zone, as suggested in the conception of the baseline geometry (secondary throat).

[Figure 12 about here.]

Figure 12b shows the absolute pressure distribution for both geometries. It is clear the design of the optimized chamber produces a better adaptation to the discharge pressure than the baseline geometry. This is better visualized with the axial distribution of pressure, Figure 13. The profile is almost equal for the shock train produced immediately after the nozzle. However, due to the enhanced design of the chamber, the sudden change produced an the end of the constant area region is not so dramatic in terms of entropy generation.

[Figure 13 about here.]

This result has a noticeable effect also on the axial distribution of the Mach number, Figure 14. The optimized geometry indicates that the normal shock wave located at the end of the constant area region is much weaker in the optimized geometry.

[Figure 14 about here.]

Regarding the entropy generation mechanisms involved, the main driving force for entropy generation is the fluctuating dissipation, with more than 90result is in accordance with our previous work [13]. The optimization procedure gives a geometry with a better design to avoid these types of losses. Entropy generation due to mean gradients and specially entropy generation due to heat transfer is completely negligible, being the calculated value lower than 2% for all the cases under study.

6. Conclusions

This study is set out to develop a methodology for the shape optimization of long-tapered ejector mixing chambers. Using such methodology, the shape optimization of an ejector mixing chamber working with R134a as operating fluid is carried out, showing an increase in entrainment ratio around 16%. This study has found that the baseline geometry produced by a one dimensional model previously developed by the authors is closely related to the optimized geometry, and constitutes an excellent baseline from which the CFD optimization can be started.

The most relevant geometrical parameter in the optimization process are the length of the variable area mixing chamber (L1), followed by the tilt angle and the length of the constant area section (L2). These changes in the geometrical parameters allow for a better re-compression along the ejector, resulting in less exergy destroyed. The main mechanism dominating entropy production inside the mixing chamber is the fluctuating dissipation for both the baseline and optimized geometry, being the entropy generation due to heat transfer negligible in all cases.

Although this study is performed with R134a, the limited ejector performance increase should be similar with others HFC or HFO based refrigerants. Further research might explore the role of the nozzle design in the overall ejector performance, and the use of different surrogate models and optimization algorithms looking for the best possible design in terms of entropy generation minimization. Additionally, the use of different turbulence models and its influence on the final design will be explored.

6.1. Reproducibility and open source policy

The authors of this work have a consistent policy of making science and engineering codes available openly, in the interest of reproducibility. The entire code and ANSYS Workbench set-up that was used to obtain the present results is available on-line from [29] and usage is licensed under CC-BY-3.0.

Acknowledgements

The authors want to acknowledge Diego Vega Bermejo and Javier Muñoz Navarro for their help in early stages of this work.

References

References

[1] J. García del Valle, J. Sierra-Pallares, P. Garcia Carrascal, and F. Castro Ruiz. An experimental and computational study of the flow pattern in a refrigerant ejector. Validation of turbulence models and real-gas effects. *Applied Thermal Engineering*, 89:795–811, 2015.

[2] J. García del Valle, J. M. Saíz Jabardo, F. Castro Ruiz, and J. F. San José Alonso. An experimental investigation of a R-134a ejector refrigeration system. *International Journal of Refrigeration*, 46:105–113, 2014.

[3] T. Sriveerakul, S. Aphornratana, and K. Chunnanond. Performance prediction of steam ejector using computational fluid dynamics: Part 1. Validation of the CFD results. *International Journal of Thermal Sciences*, 46(8):812–822, 2007.

[4] S. Croquer, S. Poncet, and Z. Aidoun. Turbulence modeling of a single-phase R134a supersonic ejector. Part 1: Numerical benchmark. *International Journal of Refrigeration*, 61:140–152, 2016.

[5] S. Croquer, S. Poncet, and Z. Aidoun. Turbulence modeling of a single-phase R134a supersonic ejector. Part 2: Local flow structure and exergy analysis. *International Journal of Refrigeration*, 61:153–165, 2016.

[6] H. Herwig and F. Kock. Direct and indirect methods of calculating entropy generation rates in turbulent convective heat transfer problems. *Heat and Mass Transfer*, 43(3):207–215, 2006.

[7] Krzysztof Banasiak, Michał Palacz, Armin Hafner, Zbigniew Buliński, Jacek Smołka, Andrzej J. Nowak, and Adam Fic. A CFD-based investigation of the energy performance of two-phase R744 ejectors to recover the expansion work in refrigeration systems: An irreversibility analysis. *International Journal of Refrigeration*, 40:328–337, 2014.

[8] Olivier Lamberts, Philippe Chatelain, and Yann Bartosiewicz. New methods for analyzing transport phenomena in supersonic ejectors. *International Journal of Heat and Fluid Flow*, 64:23–40, 2017.

[9] J. Sierra-Pallares, J. García del Valle, P. García Carrascal, and F. Castro Ruiz. A computational study about the types of entropy generation in three different R134a ejector mixing chambers. *International Journal of Refrigeration*, 63:199–213, 2016.

[10] Michal Palacz, Jacek Smolka, Waclaw Kus, Adam Fic, Zbigniew Bulinski, Andrzej J. Nowak, Krzysztof Banasiak, and Armin Hafner. CFD-based shape optimisation of a CO 2 two-phase ejector mixing section. *Applied Thermal Engineering*, 95:62–69, 2016.

[11] Michal Palacz, Jacek Smolka, Andrzej J. Nowak, Krzysztof Banasiak, and Armin Hafner. Shape optimisation of a two-phase ejector for CO 2 refrigeration systems. *International Journal of Refrigeration*, 74:212–223, 2017.

[12] Moon Soo Lee, Hoseong Lee, Yunho Hwang, Reinhard Radermacher, and Hee-Moon Jeong. Optimization of two-phase R600a ejector geometries using a non-equilibrium CFD model. *Applied Thermal Engineering*, 109:272–282, 2016.

[13] Javier Gacia del Valle, Jose M. Saiz Jabardo, Francisco Castro Ruiz, and Julio San Jose Alonso. A one dimensional model for the determination of an ejector entrainment ratio. *International Journal of Refrigeration*, 35(4):772–784, 2012.

[14] John H. Holland. *Adaptation in Natural and Artificial Systems*. The University of Michigan Press, 1st edition, 1975.

[15] D. E. Goldberg. *Genetic Algorithms in Search, Optimization and Machine Learning*. Addison-Wesley Publishing Company, 2nd edition, 1989.

[16] Felipe AC Viana, Raphael T Haftka, and Valder Steffen. Multiple surrogates: how cross-validation errors can help us to obtain the best predictor. *Structural and Multidisciplinary Optimization*, 39(4):439–457, 2009.

[17] R. Jin, W. Chen, and T. W. Simpson. Comparative studies of metamodelling techniques under multiple modelling criteria. *Structural and Multidisciplinary Optimization*, 23(1):1–13, 2001.

[18] ANSYS Inc. *DesignXplorer User's Guide*, release 18.2 edition, August 2017.

[19] Erdem Acar. Various approaches for constructing an ensemble of metamodels using local measures. *Structural and Multidisciplinary Optimization*, 42(6):879–896, 2010.

[20] Michael D McKay, Richard J Beckman, and William J Conover. Comparison of three methods for selecting values of input variables in the analysis of output from a computer code. *Technometrics*, 21(2):239–245, 1979.

[21] Jason L. Loeppky, Jerome Sacks, and William J. Welch. Choosing the sample size of a computer experiment: A practical guide. *Technometrics*, 51(4):366–376, 2009.

[22] E. W. Lemmon, M. L. Huber, and M. O. McLinder. Nist reference database 23: reference fluid thermodynamic and transport properties-refprop, version 9.1. *National Institute of Standards and Technology, Standard Reference Data Program*, 2013.

[23] Ding-Yu Peng and Donald B Robinson. A new two-constant equation of state. *Industrial & Engineering Chemistry Fundamentals*, 15(1):59–64, 1976.

[24] Ting Horng Chung, Mohammad Ajlan, Lloyd L Lee, and Kenneth E Starling. Generalized multiparameter correlation for nonpolar and polar fluid transport properties. *Industrial & engineering chemistry research*, 27(4):671–679, 1988.

[25] Federico Mazzelli and Adriano Milazzo. Performance analysis of a supersonic ejector cycle working with R245fa. *International Journal of Refrigeration*, 49:79–92, 2015.

[26] Bruce E Poling, John M Prausnitz, John P O'connell, et al. *The properties of gases and liquids*, volume 5. Mcgraw-hill New York, 2001.

[27] Adriano Sciacovelli, Vittorio Verda, and E Sciubba. Entropy generation analysis as a design tool - a review. *Renewable and Sustainable Energy Reviews*, 43:1167–1181, 2015.

[28] Edward J. Walsh and Donald McEligot. Relation of entropy generation to wall laws for turbulent flows. *International Journal of Computational Fluid Dynamics*, 22(10):649–657, 2008.

[29] José' Sierra-Pallares. Uvaejector: Cfd modelling of refrigerant ejectors. Mendeley Data, v1, 2018.

List of Figures

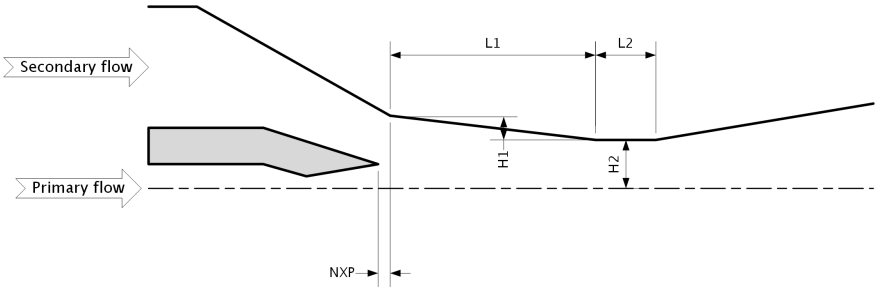

Figure 1: Baseline geometry along with its geometrical variables

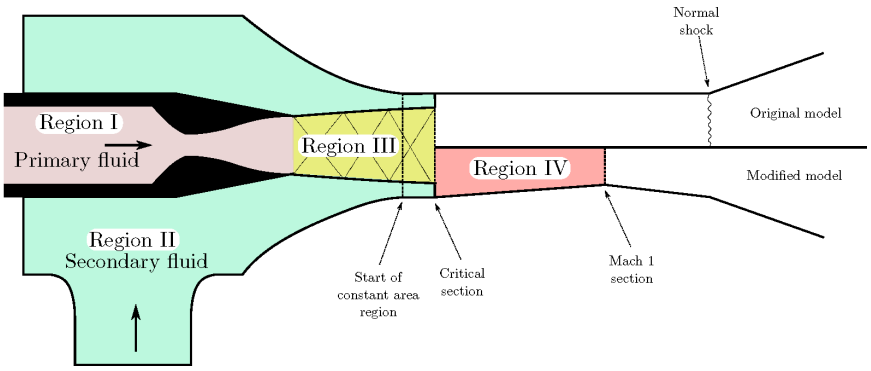

Figure 2: Design parameters of the baseline geometry.

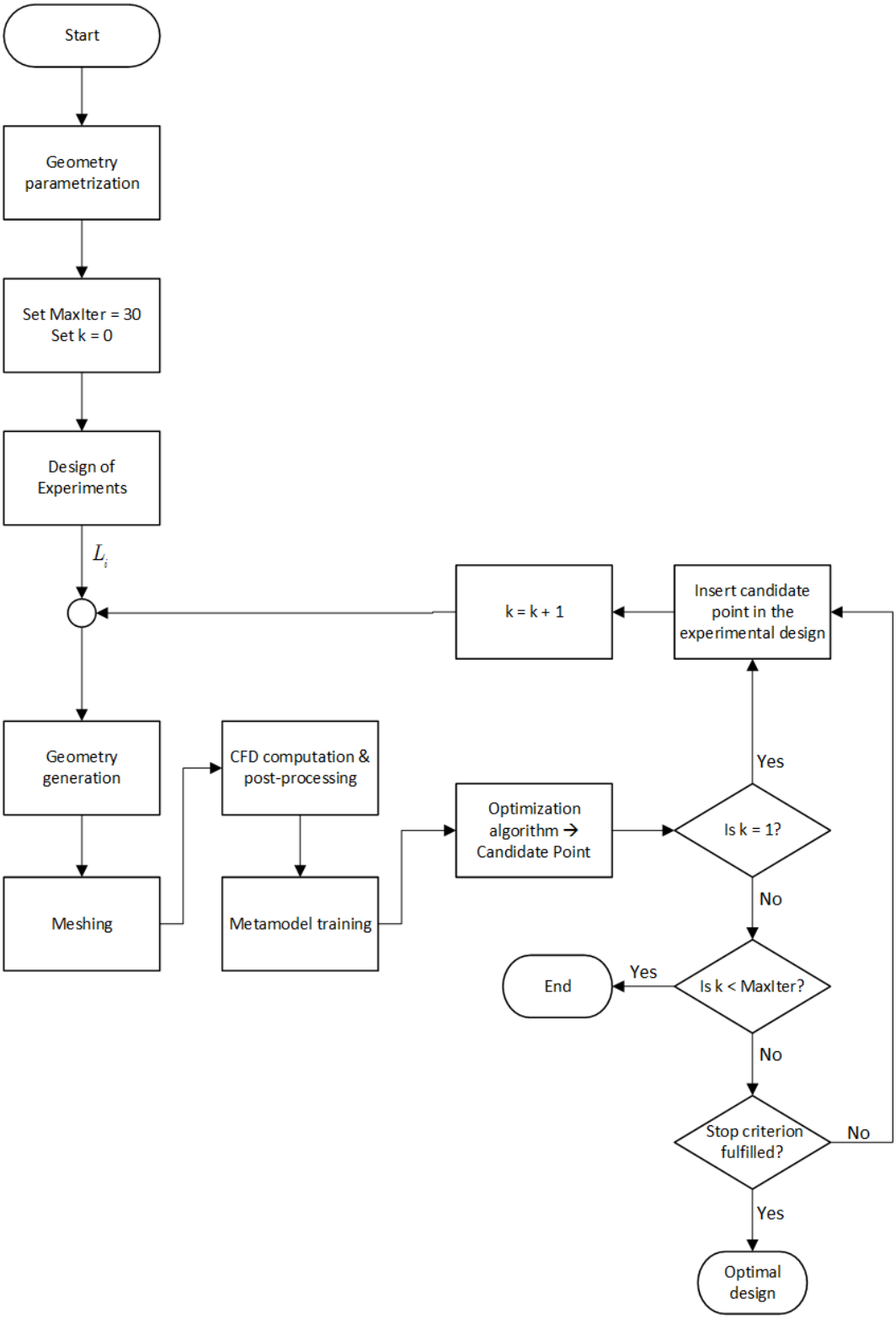

Figure 3: Workflow for the online shape optimization employed in this work

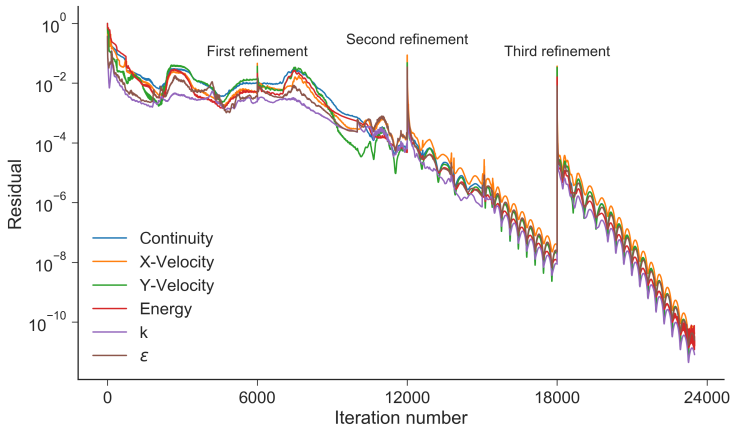

(a)

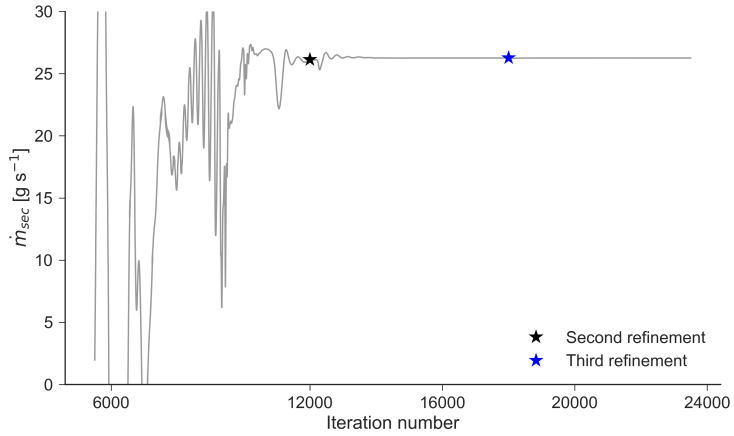

(b)

Figure 4: (a) Residuals obtained by ANSYS Fluent, (b) Secondary flow rate Vs. iteration number. Baseline geometry with critical boundary conditions as prescribed in Table X

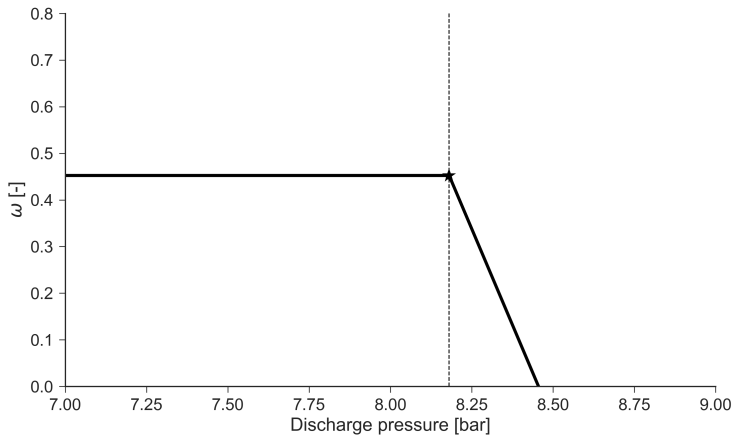

(a)

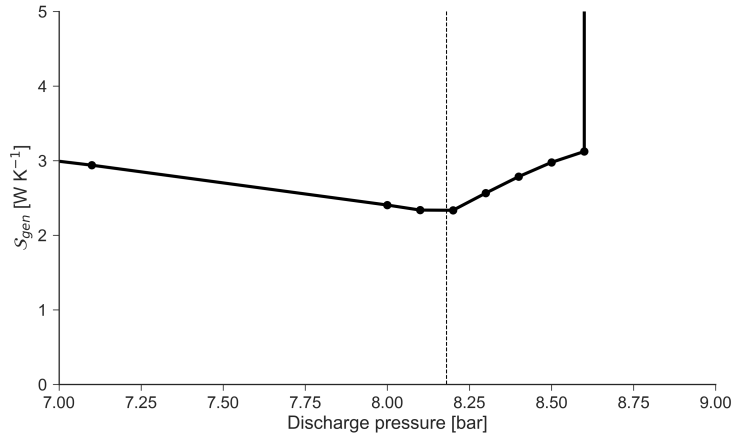

(b)

Figure 5: (a) Entrainment ration Vs. Discharge pressure and (b) Entropy generated Vs. Discharge pressure for the baseline geometry

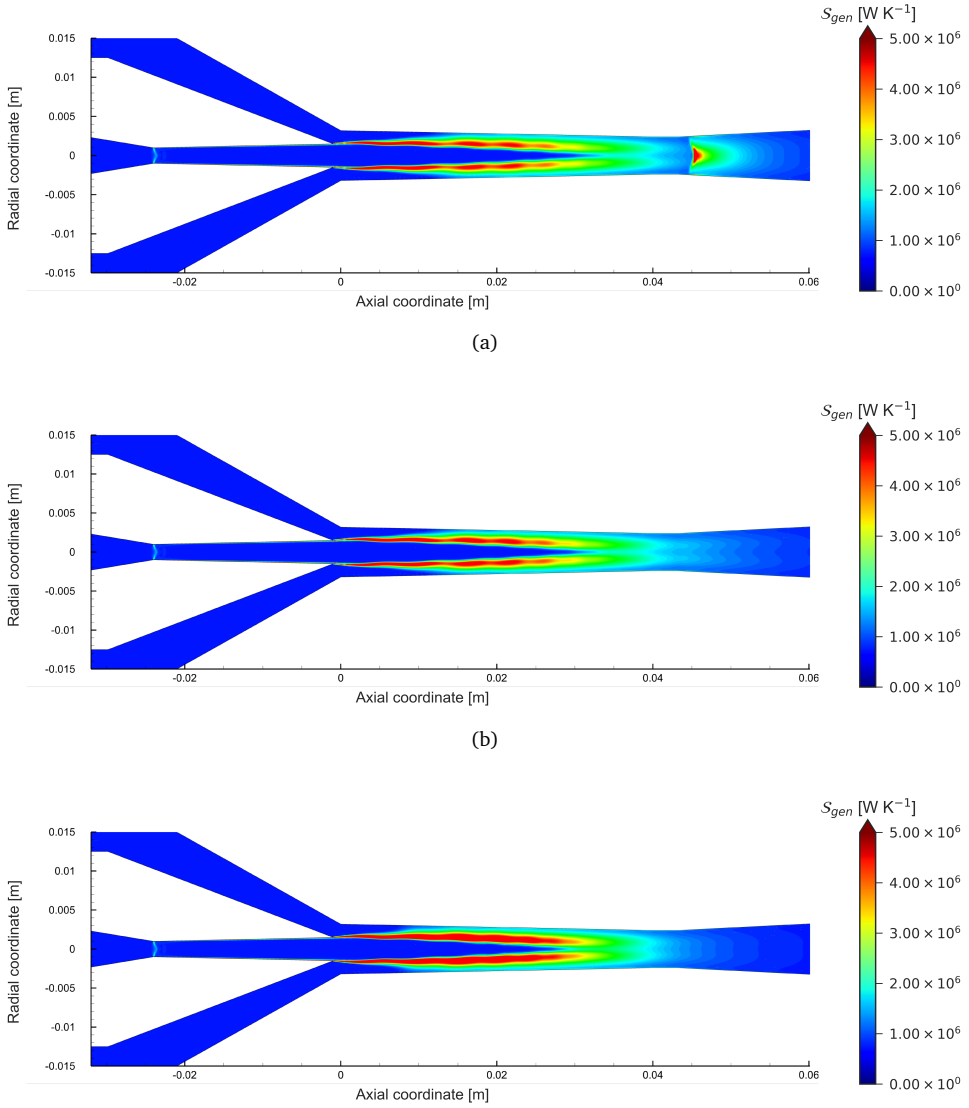

Figure 6: Entropy generation contour maps for (a) On - design conditions, (b) Critical conditions, (c) Off - design conditions

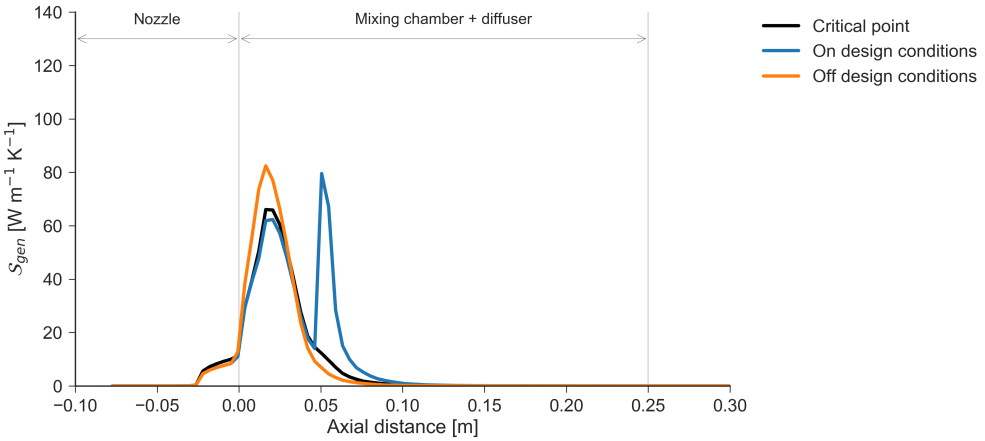
Nozzle
Mixing chamber + diffuser
Critical point
On design conditions
Off design conditions
S_{gen} [W m^{-1} K^{-1}]
Axial distance [m]
140
120
100
80
60
40
20
0
−0.10
−0.05
0.00
0.05
0.10
0.15
0.20
0.25
0.30

Figure 7

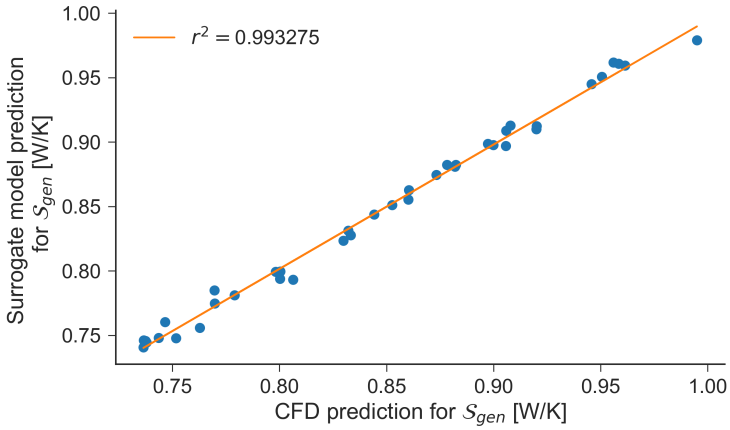

Figure 8: Goodness of fit of the surrogate model

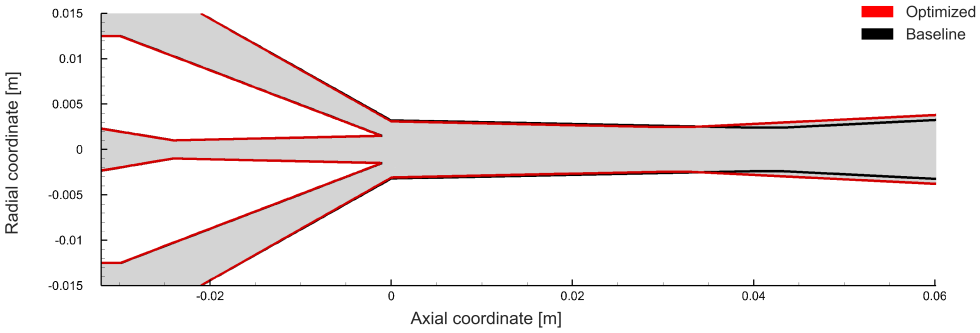

Figure 9: Comparison between the baseline and optimized geometry

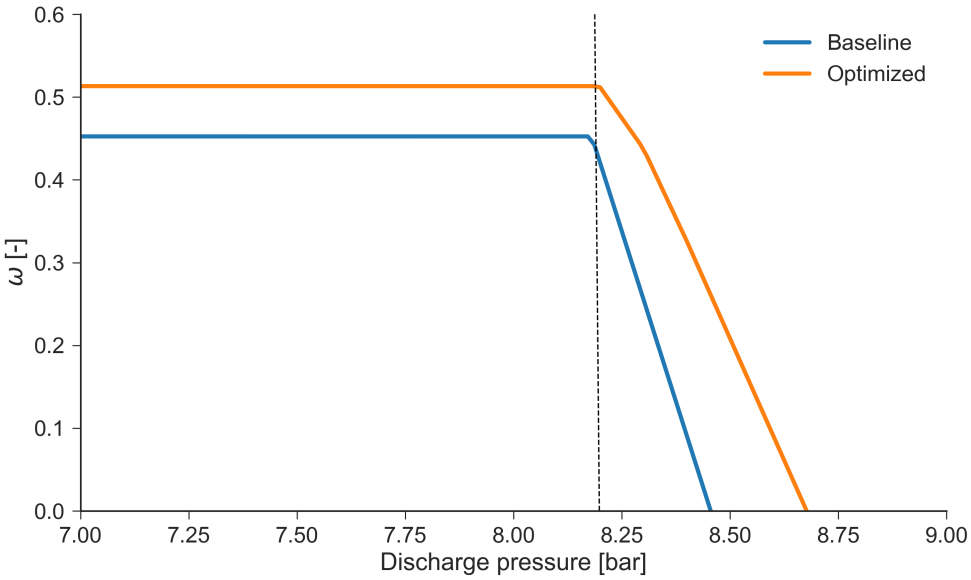

Figure 10: Entrainment ratio for the baseline and optimized geometries

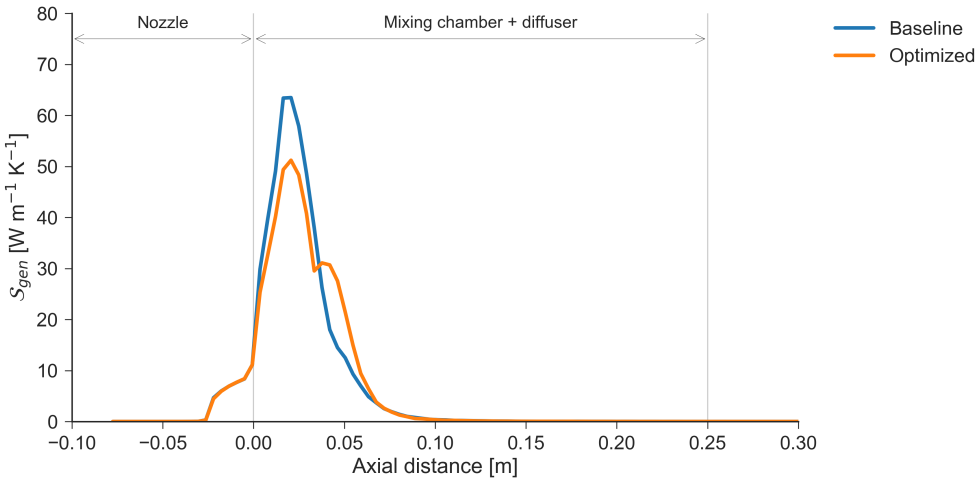

Figure 11: Axial entropy generation rate for the baseline and optimized geometries

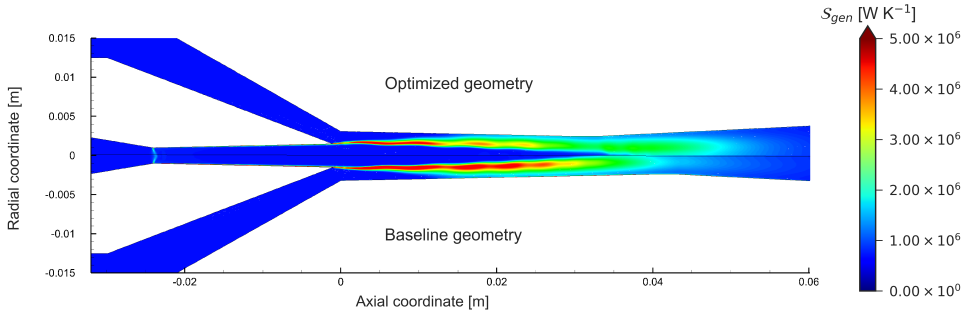

(a)

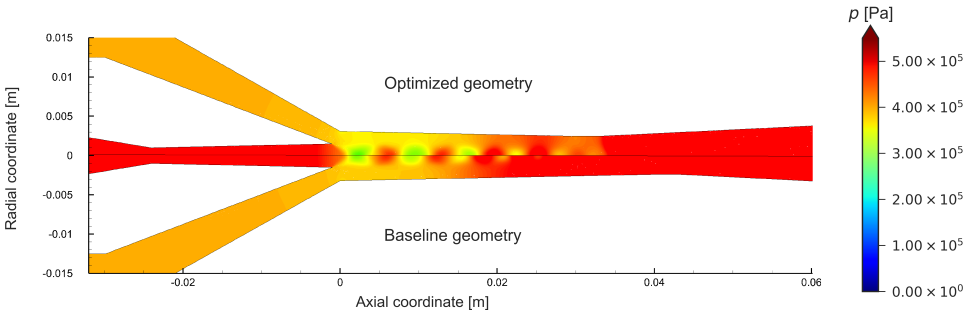

(b)

Figure 12: (a) Entropy generation contour maps for the baseline and optimized geometries and (b) pressure contour maps.

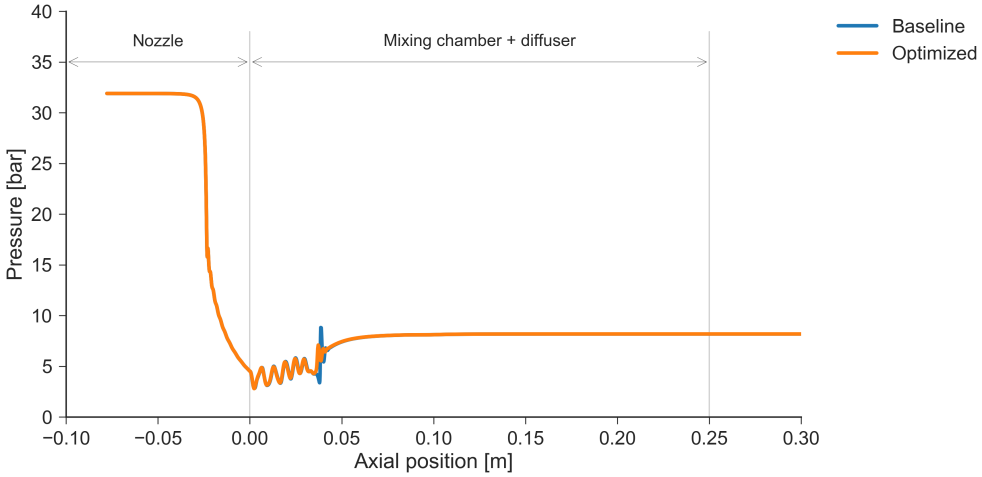

Figure 13: Absolute pressure along axial position. Baseline Vs. optimized geometry

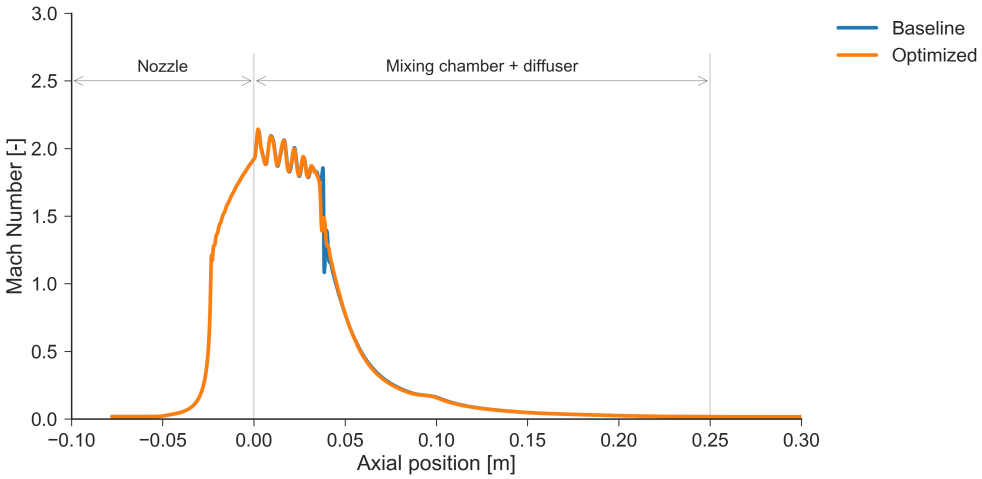

Figure 14: Mach number along axial position. Baseline Vs. optimized geometry

List of Tables

Table 1: Boundary conditions for the primary and secondary streams

Boundary	Total pressure [bar]	Total temperature [K]
Primary	31.90	373
Secondary	4.15	293

Table 2: Baseline geometry parameters

Name	NXP [mm]	L1 [mm]	H1 [mm]	L2 [mm]	H2 [mm]
Baseline	1.00	40.00	0.80	3.20	2.40

Table 3: Baseline geometry parameters and design space limits

Name	NXP [mm]	L1 [mm]	H1 [mm]	L2 [mm]	H2 [mm]
Baseline	1.00	40.00	2.40	3.20	0.80
Upper limit	1.20	48.00	2.88	3.84	0.96
Lower limit	0.80	32.00	1.92	2.56	0.64

Table 4: DoE along with entropy generation and secondary flow rate. Baseline case is included

Name	NXP [mm]	L1 [mm]	H1 [mm]	L2 [mm]	H2 [mm]	$\dot{S}_{gen}$ [W K^{-1}]	$\dot{m}$ [kg s^{-1}]
Baseline	1.000000	40.000000	0.800000	3.200000	2.400000	2.308904	0.018419
E1	1.028000	32.160000	0.828800	3.340800	2.582400	2.883933	0.003479
E2	1.140000	32.480000	0.764800	3.238400	2.006400	2.760417	0.008345
E3	1.188000	32.800000	0.681600	3.520000	2.544000	2.532492	0.013431
E4	0.892000	33.120000	0.880000	3.468800	2.083200	2.645846	0.009739
E5	0.964000	33.440000	0.688000	2.828800	2.467200	2.209587	0.021335
E6	0.996000	33.760000	0.912000	2.700800	2.352000	2.394468	0.017513
E7	1.196000	34.080000	0.886400	3.289600	2.025600	2.723494	0.007606
E8	0.852000	34.400000	0.668800	2.880000	2.294400	2.418959	0.017279
E9	0.916000	34.720000	0.809600	3.033600	2.736000	1.995980	-0.013586
E10	0.948000	35.040000	0.771200	3.417600	2.217600	2.489631	0.014220
E11	0.836000	35.360000	0.867200	3.212800	2.121600	2.619693	0.010555
E12	1.076000	35.680000	0.784000	2.752000	2.755200	8.900349e+07	-0.016169
E13	0.876000	36.000000	0.662400	3.648000	2.870400	1.137657e+10	-0.022794
E14	0.804000	36.320000	0.752000	2.956800	2.064000	2.647004	0.009523
E15	1.108000	36.640000	0.758400	2.854400	2.428800	2.239728	0.020287
E16	1.124000	36.960000	0.841600	3.699200	2.486400	2.717117	0.008395
E17	1.052000	37.280000	0.745600	3.622400	2.390400	2.309421	0.019288
E18	0.980000	37.600000	0.899200	2.931200	2.179200	2.581277	0.011633
E19	0.828000	37.920000	0.732800	2.649600	2.851200	3.837599	-0.022727
E20	0.972000	38.240000	0.835200	3.008000	2.524800	2.984955	0.001111
E21	1.156000	38.560000	0.892800	2.726400	2.236800	2.557741	0.013240
E22	1.092000	38.880000	0.854400	3.059200	2.793600	9.727745e+05	-0.034099
E23	1.036000	39.200000	0.713600	3.750400	2.832000	2.666840e+05	-0.021580
E24	0.908000	39.520000	0.726400	3.084800	2.256000	2.499893	0.015022
E25	0.812000	39.840000	0.707200	3.673600	2.371200	2.337016	0.018757
E26	0.956000	40.160000	0.860800	3.110400	2.448000	2.759865	0.007105
E27	1.180000	40.480000	0.937600	3.494400	2.678400	7.705467e+04	-0.019499
E28	1.060000	40.800000	0.656000	2.777600	2.313600	2.400810	0.017153
E29	0.988000	41.120000	0.777600	3.801600	1.948800	2.867663	0.004493
E30	0.860000	41.440000	0.956800	3.443200	2.198400	2.634603	0.010926
E31	1.172000	41.760000	0.803200	3.366400	2.275200	2.496473	0.014414
E32	0.844000	42.080000	0.675200	3.187200	2.140800	2.580599	0.011325
E33	1.068000	42.400000	0.931200	3.724800	2.774400	1.649067e+05	-0.027402
E34	1.012000	42.720000	0.816000	3.827200	2.044800	2.717490	0.006723
E35	1.132000	43.040000	0.944000	3.571200	2.160000	2.692118	0.009228
E36	0.884000	43.360000	0.950400	3.315200	2.812800	1.029150e+05	-0.031725
E37	0.940000	43.680000	0.848000	2.982400	2.620800	1.401625e+05	-0.015278
E38	1.004000	44.000000	0.822400	2.675200	2.102400	2.699692	0.008316
E39	1.100000	44.320000	0.739200	2.572800	1.968000	2.851753	0.004903
E40	1.116000	44.640000	0.700800	2.905600	2.716800	2.445210e+09	-0.017083
E41	0.868000	44.960000	0.796800	3.776000	2.697600	3.837040	-0.019427
E42	1.084000	45.280000	0.873600	2.598400	2.659200	1.052953e+10	-0.019903
E43	0.820000	45.600000	0.720000	3.136000	2.332800	2.401221	0.016375
E44	0.900000	45.920000	0.924800	3.545600	2.640000	1.429970e+04	-0.019932
E45	1.020000	46.240000	0.905600	2.803200	2.409600	3.073574	-0.000621
E46	1.044000	46.560000	0.694400	3.161600	1.929600	2.874988	0.003841
E47	0.924000	46.880000	0.918400	2.624000	2.505600	2.399856e+05	-0.011882
E48	1.148000	47.200000	0.649600	3.392000	2.601600	1.597908e+05	-0.007904
E49	0.932000	47.520000	0.790400	3.596800	1.987200	2.837166	0.004378
E50	1.164000	47.840000	0.643200	3.264000	2.563200	3.166809	-0.003324

Table 5: On-line optimization for the DoE around the baseline geometry

Name	NXP [mm]	L1 [mm]	H1 [mm]	L2 [mm]	H2 [mm]	$\mathcal{S}_{gen}$ [W K^{-1}]	$\dot{m}$ [kg s^{-1}]
E51	1.050024	32.289292	0.699433	2.709810	2.410726	2.288263	0.020352
E52	0.916037	34.270608	0.703742	2.680309	2.435241	2.230624	0.020957
E53	0.894014	34.723859	0.675580	2.723698	2.454672	2.212302	0.021637
E54	0.879998	32.468606	0.674580	2.689832	2.429169	2.255019	0.020920
E55	0.964323	33.034327	0.687594	2.758000	2.462447	2.213765	0.021554
E56	0.869297	32.524856	0.691448	2.722060	2.451055	2.209264	0.021428

Table 6: Differences between the baseline and the optimized geometry (E56)

Name	NXP [mm]	L1 [mm]	H1 [mm]	L2 [mm]	H2 [mm]	$\mathcal{S}_{gen}$ [W K^{-1}]	$\dot{m}$ [kg s^{-1}]
Baseline	1.000000	40.000000	0.800000	3.200000	2.400000	2.308904	0.018419
E56	0.869297	32.524856	0.691448	2.722060	2.451055	2.209264	0.021428